INSTITUTE OF PHYSICS PUBLISHING and INTERNATIONAL ATOMIC ENERGY AGENCY NUCLEAR FUSION

Nucl. Fusion **45** (2005) S291–S297 doi:10.1088/0029-5515/45/10/S25

Power plant design and accelerator technology for heavy ion inertial fusion energy

B.Yu. Sharkov[1,a], N.N. Alexeev[1], M.M. Basko[1], M.D. Churazov[1], D.G. Koshkarev[1], S.A. Medin[2], Yu.N. Orlov[3] and V.M. Suslin[3]

[1] Institute for Theoretical and Experimental Physics, B. Cheremushkinskaya 25, 117259 Moscow, Russia
[2] Institute for High Energy Densities, RAS, Izhorskaya 13/19, 125412 Moscow, Russia
[3] Keldysh Institute for Applied Mathematics, RAS, Miusskaya 4, 125047 Moscow, Russia

E-mail: boris.sharkov@itep.ru

Received 22 December 2004, accepted for publication 23 March 2005
Published 7 October 2005
Online at stacks.iop.org/NF/45/S291

Abstract
The concept of a power plant for fast-ignition heavy ion fusion is developed. It is based on repetitive detonation of a cylindrical direct-drive target, producing 750 MJ of fusion yield in each microexplosion. A heavy-ion driver system providing consequent compression and ignition of the cylindrical DT target is described. Data on energy fluxes generated by the microexplosion are given. The design of the thin liquid wall reactor chamber is presented. The behaviour of the liquid film at the first wall and the blanket coolant and material under a pulsed energy flux loading is analysed. The energy conversion thermal scheme and power plant output parameters are presented. The state of the art at the ITEP-TWAC experimental accelerator is described.

PACS numbers: 52.58.Hm, 28.52.Av, 52.57.Fg

1. Introduction

For inertial fusion energy, heavy ion beams represent a highly attractive approach to driving the targets in a practical electricity-generating power plant. The decisive factors determining the choice of the heavy ion driver are high accelerator efficiency and sufficiently large target gain. These are the conditions providing high efficiency of the power plant. The HYLIFE-II concept [1, 2] employs a linear induction 10 GeV-heavy-ion driver, indirect drive target and thick liquid wall reactor chamber. In this concept the reactor chamber materials problem is practically eliminated at the cost of optimal organization of liquid jets dynamic pocket.

An alternative concept of a heavy ion fusion power plant has been proposed in [3, 4]. This concept is based on a 100 GeV-heavy-ion driver, direct drive of a cylindrical target in the fast ignition mode and a blanket with a thin-liquid first wall. Such an approach is characterized by a simple driver–reactor chamber interface and by a moderate value of the required target gain. The problems of the fast-ignition heavy ion fusion (FIHIF) concept are related to the rigid physical conditions of the fast-ignition scenario and the length of the heavy ion driver.

In this paper new data on the target energy release and the reactor chamber response, obtained using the numerical codes developed, are given. The output parameters of the FIHIF power plant are updated.

Recent experimental results on the IFE related accelerator physics and technology issues obtained using a newly commissioned ITEP-TWAC facility are discussed.

2. Ground plan and high-power driver

The ground plan of the proposed FIHIF power plant is outlined in figure 1. The length of the main linac is of the order of 10 km. The diameter of the storage and compression rings is 1 km. The area occupied by the reactor and turbogenerator building, as well as the cooling towers, is of the same order of magnitude.

The driver consists of the following main parts [4]: ion sources for four Pt isotopes with the plus and minus charge states are arranged in eight groups of four devices each.

In the main linac the ion energy is increased to 100 GeV. After this the ions with different charges and masses are separated into eight beams, which are compressed in two stages—in storage rings and in exit sections by the time-of-flight method. The final collection of eight beams in an individual transfer line results in a single bunch of 0.2 ns

[a] Author to whom any correspondence should be addressed.

 © 2005 IAEA, Vienna Printed in the UK

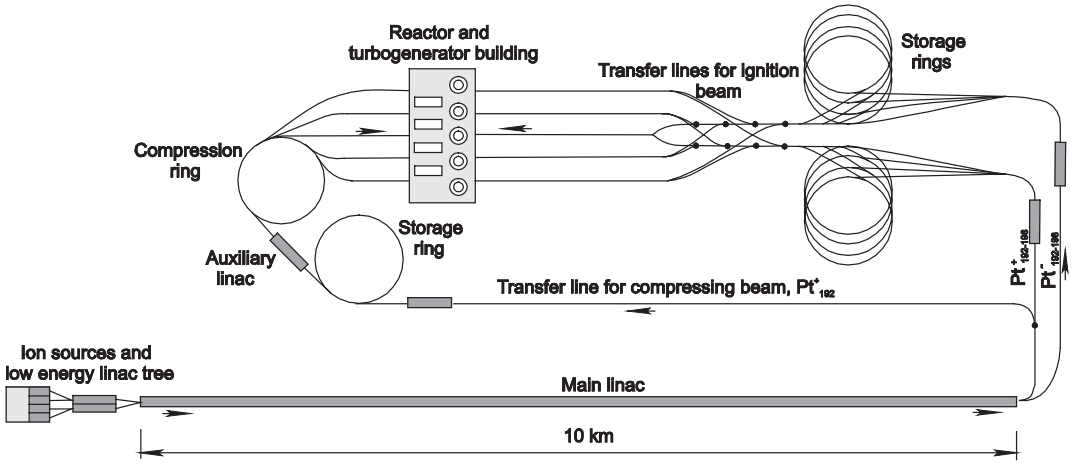

Figure 1. Ground plan outline for FIHIF power plant.

Table 1. General parameters of FIHIF driver.

Ions	$Pt^{+,-}_{192,194,196,198}$
Ion energy (GeV)	100
Hollow compression beam	
Energy (MJ)	7.1
Duration (ns)	75 (profiled)
Maximum current (kA)	1.6
Rotation frequency (GHz)	1
Rotation radius (mm)	1.33–1.89
Focal spot radius (mm)	0.65–1.33
Ignition beam	
Energy (MJ)	0.4
Duration (ns)	0.2
Max. current (kA)	20
Spot radius (μm)	50
Linac	
Main linac length (km)	10
Repetition rate (Hz)	8
Driver efficiency	0.25

duration delivered to the compressed target. The preliminary compression of the target is accomplished by the hollow beam which carries only Pt^{+}_{192} ions. This beam is temporally profiled over a duration of 75 ns with a maximum current of 1.6 kA. The general parameters of the FIHIF driver are given in table 1.

The theoretical scheme of the non-Liouvillian beam compression to 200 ps with a power of 2 PW was described in [17].

The repetition rate of the FIHIF driver is taken as 8 Hz, which provides two shots per second in each of the four reactor chambers. The evaluated nominal driver efficiency is equal to 0.25. The operational characteristics of the driver equipment appear to be feasible on the basis of the present day accelerator technologies.

3. Cylindrical target

In the present scenario, because of the relatively long ranges (5–10 g cm^{-2}) of 100 GeV heavy ions, we are compelled to use a cylindrical rather than a spherical target. Our target consists of a DT cylinder with a radius of 0.112 cm and a length of 0.71 cm, surrounded by a lead shell with a radius of 0.4 cm

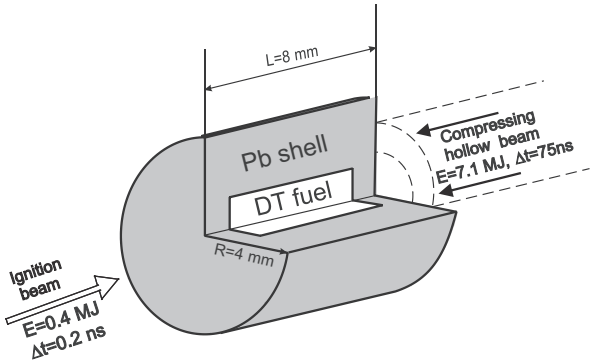

Figure 2. Cylindrical target for the FIHIF concept.

(see figure 2). The target ends are sealed with sufficiently thin lead walls that can be easily penetrated by the igniting beam at the end of the compression stage. The masses of the DT fuel and lead are equal to 5.6 mg and 4.44 g, respectively. The length of the target is matched to the stopping range of 100 GeV Pt^{+}_{192} ions deposited by the compression beam.

The relative inefficiency of the cylindrical implosion is partly compensated by using direct drive. A high degree of azimuthal uniformity of the ion energy deposition, needed for direct drive, is ensured by fast rotation of the compression beam around the target axis, so that the beam heats a ring area of the lead shell outside the DT/lead interface. A recent study [5] has shown that 8–10 beam revolutions per main pulse should be sufficient to obtain the needed radial convergence.

The target parameters and performance have been optimized in two separate series of simulations (one dimensional for the compression, and two dimensional for the ignition stage), as described in more detail in [6]. The Rayleigh–Taylor instability at the compression stage is mitigated by a shallow density gradient [7], which is naturally formed due to the tangential (with respect to the accelerated interface) irradiation of an initially uniform absorber layer. To minimize the beam energy losses due to the absorber rarefaction, different radii of the beam focal spot, $r_{\rm f}$, and of the beam rotation orbit, $r_{\rm b}$, were used for the prepulse and the main pulse, namely, $r_{\rm f} = 1.33$ mm, $r_{\rm b} = 2.55$ mm for the prepulse and $r_{\rm f} = 0.65$ mm, $r_{\rm b} = 1.89$ mm for the main pulse.

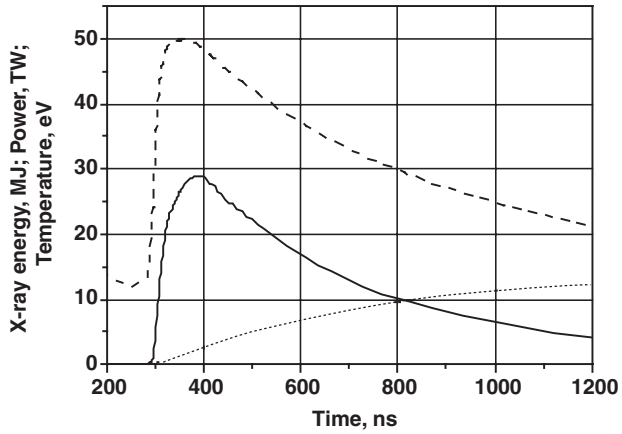

Figure 3. Temporal profiles of the characteristics of the x-ray pulse from the FIHIF cylindrical target. Dashed curve, temperature; solid curve, power; dotted curve, energy.

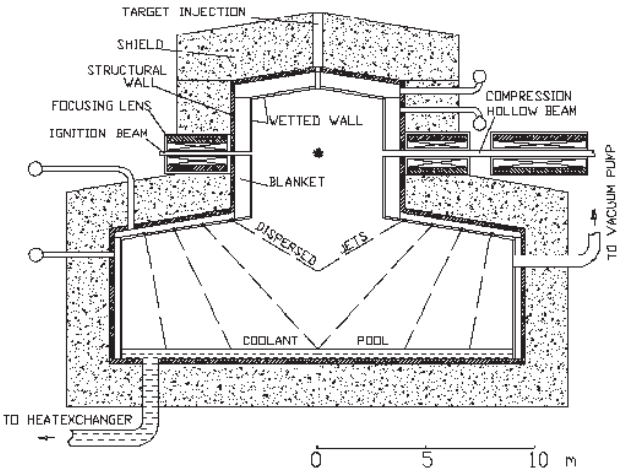

Figure 4. Reactor chamber for the FIHIF power plant.

The evaluated burn fraction amounts to 0.39, which corresponds to a fusion yield of 750 MJ and an energy gain of 100. The output energy is partitioned into 580 MJ in neutrons, 154 MJ in flying debris and 17 MJ in x-rays.

Hard x-rays from the DT burn are processed by a massive lead shell into a much softer radiation. This causes the decrease in the x-ray temperature and the delay and lengthening of the final x-ray pulse which are shown in figure 3. The duration of this pulse is quite long and exceeds 0.7 μs; the mean x-ray temperature is equal to 30 eV.

4. Reactor chamber design

The general design of the reactor chamber is shown in figure 4. The chamber consists of two cylindrical sections: the upper smaller section in which the target explosion takes place, and the lower section in which sprayed jets of coolant are injected. The diameters of these sections are 8 m and 16 m, respectively. Such a configuration prevents overpressurization after the microexplosion and ensures a high rate of vapour condensation on sprayed jets.

The coolant is eutectic $Li_{17}Pb_{83}$ at a temperature of 823 K. The saturation vapour density which corresponds to this temperature is $10^{18}\,m^{-3}$ [8]. Under these conditions, the Pt ion beam is not degraded by the atmosphere in the reactor chamber.

The first wall and the blanket are of conventional design. The liquid film is formed on a porous SiC wall. In the blanket, the tubing is made of vanadium alloy. The structural wall is composed of HT-9 steel.

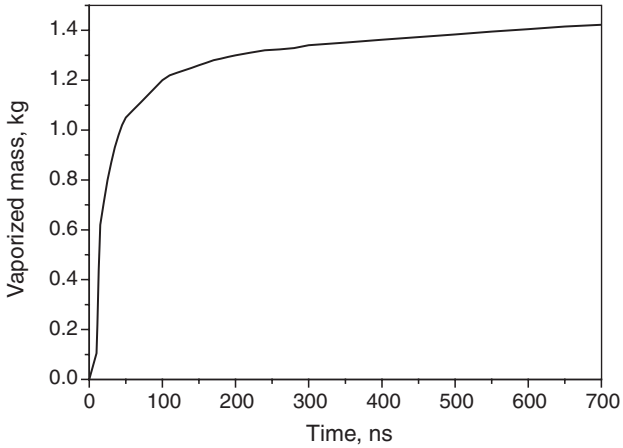

Figure 5. Temporal variation of vaporized mass in reactor chamber during x-ray deposition.

5. Liquid film response to x-rays and ion debris

We suppose that the x-ray pulse has a Planckian spectrum with the temperature and power depending on time as shown in figure 3. The response of the thin-liquid protecting layer to x-rays has been simulated numerically using a Lagrangian one-dimensional hydrodynamic code in cylindrical geometry. This code solves the equations of mass, momentum and energy conservation, which include viscosity and heat transfer. The energy deposition by x-ray radiation in the film is computed using the mass attenuation coefficient for eutectic $Li_{17}Pb_{83}$ determined with the use of individual substances' data, depending on the photon energy, given in [9]. The wide-range equation of state is taken from [10] only for lead, because the presence of lithium is neglected for the thermodynamic properties. In this equation of state the vaporization and the first ionization of lead are taken into account.

The deposition of x-rays occurs in the thin liquid layer at the first moments of time, and later in vapour, which expands from the liquid surface. The rate of vaporization strongly depends on the x-ray intensity.

After 100 ns the vaporization rate begins to fall despite the fact that the x-ray intensity continues to rise. This is caused by the intensive absorption of x-ray radiation by vapour and demonstrates a screening effect of the vapour layer. The total vaporized mass by the end of the x-ray pulse is some 1.42 kg (see figure 5).

The vaporization process is accompanied by the generation of a shock wave in the liquid film. This shock is relatively weak and travels across the film with the velocity of sound, approximately equal to $2000\,m\,s^{-1}$ (see figure 6). It crosses the film of 2 mm width in 1 μs and arrives at the first wall with an amplitude of 250 MPa. The tail pressure

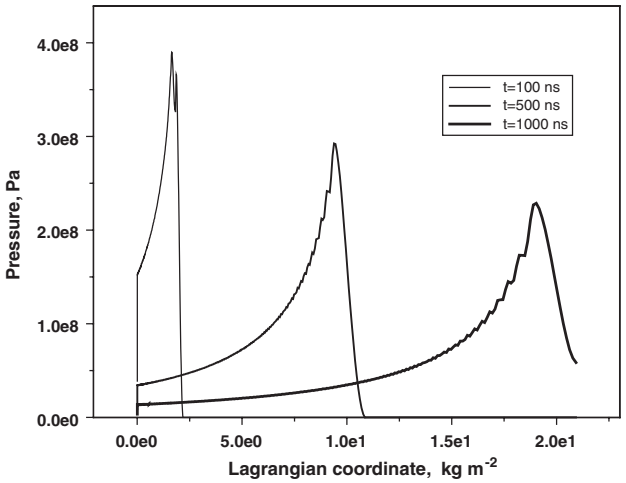

Figure 6. Shock wave propagation in the liquid film.

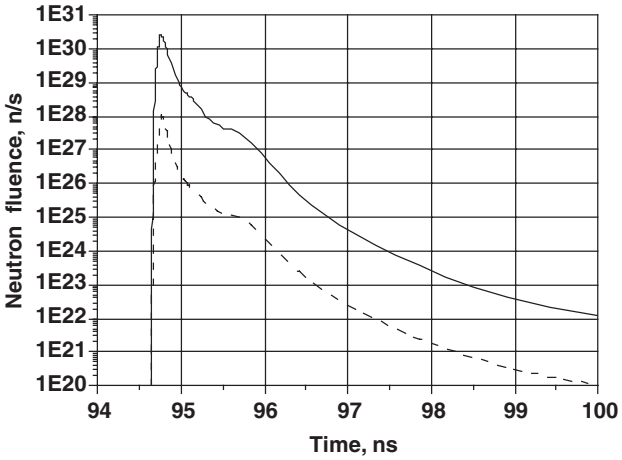

Figure 7. Neutron pulse of the FIHIF target microexplosion. Solid line, 14 MeV; dotted line, 2.45 MeV.

of the pressure pulse is equal to the saturation pressure at the vaporization front. It is seen that the saturation pressure decreases in time.

The pressure at the vaporization front determines the impulse transmitted to the first wall during the time interval $\tau = 1000$ ns. It turns out to be equal to $I = 64$ Pa s. For the case when the first wall is considered as a thin spherical shell, deformed by this instantaneous impulse, the corresponding displacement of the porous SiC first wall is computed to be equal to 4×10^{-6} m. Then the maximum pressure on its external surface in contact with the coolant amounts to $P_{10} = 14$ MPa. We take the elasticity limit of the SiC porous wall to be equal to $Y_0 = 35$ MPa. Since the radial stress, P_{10}, turns out to be below the elasticity limit, Y_0 (the von Mises criterion), we conclude that the first wall remains in the elasticity deformation region under this loading.

The target debris approaches the vapour layer at 10 μs. The interaction of the debris flow with the vapour layer is determined by the stopping range of 80 keV ions of lead, which is equal to 6×10^{-6} g cm^{-2} according to the Bethe–Bloch formula for the Coulomb energy losses [11]. Thus the stopping range is much smaller then the vapour layer width. Therefore it can be assumed that the evaporated coolant is additionally superheated by debris ions. The evaluated resulting temperature of vapour amounts to 230 eV (approximately equal to 2.5×10^6 K) in [4]. Revaporization results in additional evaporated coolant mass. The process of additional vaporization and condensation is considered to start with this initial temperature of vapour. The evaporation–condensation processes are described by kinetic relationships [12] in the same way as in [4]. Revaporization results in the additional evaporated coolant mass of 14 kg. The rate of the following condensation is mainly determined by the large surface of the jet droplets in the lower part of the reactor chamber (4.5×10^4 m^2 for a total mass of 7000 kg per shot).

The vapour density practically reaches the saturation value at 0.1 s. This indicates that the condensation process would not limit the repetition rate of shots. Apparently, the actual limitation will be the rate of liquid droplets clean-up. In the case of free gravity precipitation the repetition rate cannot exceed 2 Hz.

Table 2. Blanket structure and energy deposition in the zones.

Zone	Matter	Radius (cm)	Energy density (MJ m^{-3})	Temperature rise (K)
1	PbLi	400.0	23.8	13.0
2	SiC + PbLi	400.2	20.7	5.1
3	PbLi	401.0	18.5	11.1
4	V_4Cr_4Ti	407.0	8.9	2.8
5	PbLi	407.4	12.2	7.3
6	V_4Cr_4Ti	413.4	6.1	1.7
7	PbLi	413.8	6.5	4.0
8	V_4Cr_4Ti	419.8	2.8	0.9
9	PbLi	420.2	4.1	2.0
10	V_4Cr_4Ti	426.2	1.1	0.5
11	PbLi	426.6	1.5	0.9
12	V_4Cr_4Ti	432.6	0.8	0.2
13	PbLi	433.0	0.9	0.4
14	V_4Cr_4Ti	439.0	0.2	0.1
15	PbLi	439.4	0.3	0.2
16	V_4Cr_4Ti	445.4	0.1	0.05
17	HT-9	446.4	0.07	0.01
18	Concrete	452.0	—	—

6. Neutron heating of blanket

The neutron pulse generated by the microexplosion is shown in figure 7 according to [6]. The duration of the effective burning is equal to approximately 1 ns, so we can treat the heating of the blanket as instantaneous.

The neutron spectrum is evaluated by steady-state calculations with the use of the MCNP code [13] in spherical approximation for the moment of the central peak of the neutron pulse. The mean neutron energy is equal to 12.2 MeV.

The blanket has the structure of a multi-layer cylinder whose composition is given in table 2. The total blanket and structural wall thickness is equal to 52 cm. The blanket zones and the inner radii are counted from the surface of the protecting liquid layer. The scheme of coolant motion through the vanadium tubes is shown in figure 8. In this scheme vanadium tubes are represented as thin black vertical lines, the direction of coolant flow is designated by arrows and HT-9 stainless steel is shown as the thick grey stripe on the right-hand side of this scheme. The dimensions of these blanket zones are given in table 2.

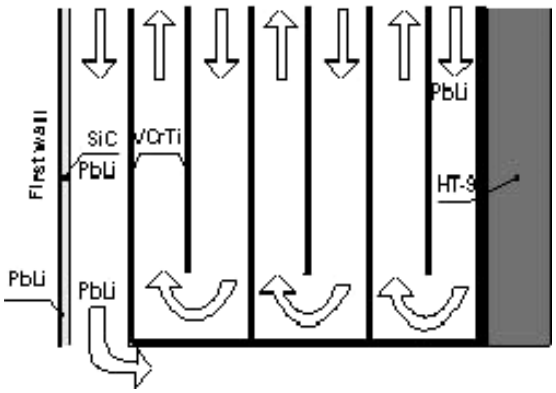

Figure 8. Scheme of coolant motion through the vanadium tubes.

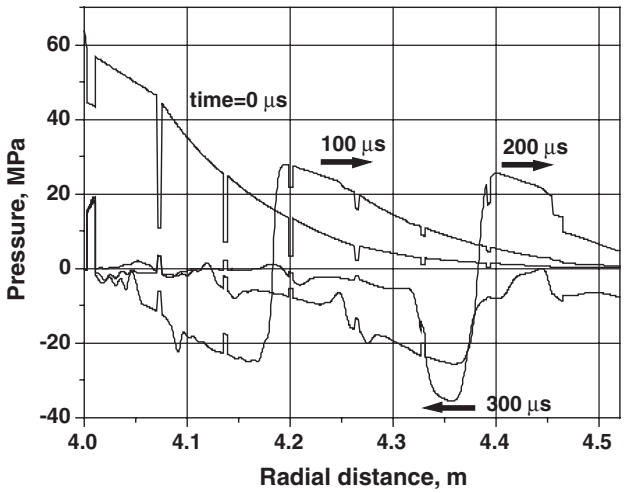

Figure 9. Pressure distribution in the blanket and in the structural wall of the FIHIF reactor chamber at different times.

Two-dimensional calculations of neutron transport in the blanket using the MCNP code resulted in high energy release in the materials (see table 2). The tritium breeding ratio (TBR) for this blanket is equal to 1.112, and the blanket multiplication factor is evaluated as 1.117. The neutron yield of 580 MJ is enhanced in the blanket to 647 MJ. Hence, the total energy release per shot is 818 MJ.

Neutron heating generates a pressure/stress pulse, which travels across the blanket and refracts at the contact surfaces. For evaluation of the material loading under conditions of neutron energy release one-dimensional hydrodynamic equations in cylindrical geometry are solved. The computational domain includes the blanket, structural wall and concrete shield. Free adiabatic boundary conditions were used. The initial distributions were uniform for all the parameters, except for the internal energy, which was determined from neutronics computations. The data for solid materials, silicon carbide, vanadium alloy and stainless steel are given by Zinkle in [14]. The properties of the $Li_{17}Pb_{83}$ eutectic are taken from [15]. The equation of state is taken in the Mie–Gruneisen form. The Gruneisen coefficient, Γ, is projected to be 2 for the SiC porous wall, stainless steel and concrete.

In figure 9 the radial pressure distribution in the blanket and the structural wall is plotted for different times. The right boundary is the contact interface between the stainless steel and concrete. The frequency of the main pulsations of the deviatoric radial stress, S_{rr}, in the structural walls is 2.3 kHz. The maximum values of S_{rr} in the first vanadium wall alloy do not exceed 11 MPa, which is much less than the elastic limit, 129 MPa. The main pulsation is modulated by a low frequency, which may be caused by reflection of the refracted pulse from the concrete.

Table 3. Parameters of thermal loops of FHIF power plant.

First loop	
Coolant	LiPb
Mass flow rate (kg s^{-1})	13 063
Pump power (kW)	11 584
Second loop	
Coolant	Na
Mass flow rate (kg s^{-1})	6402
Pump power (kW)	3768
Steam cycle	
Mass flow rate (kg s^{-1})	548.7
Inlet pressure (MPa)	18
Superheat pressure (MPa)	3
Condenser pressure (MPa)	0.009
Turbine efficiency	0.875
Steam cycle efficiency	0.417
Reactor	
Fusion power (MW)	1500
Driver power (MW)	60
Neutron power ratio	0.773
Blanket multiplication	1.117
Power plant	
Thermal efficiency	0.407
Net efficiency	0.373
Net power output (MW)	626

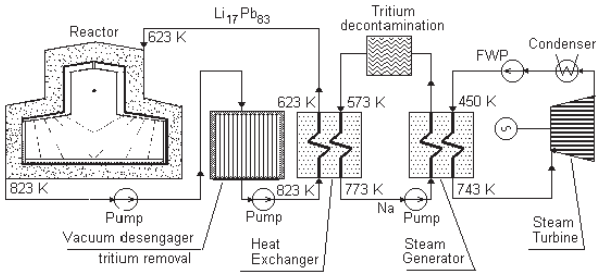

Figure 10. Thermal scheme for FIHIF power plant.

7. Energy conversion and the plant energy balance

The energy conversion system consists of three loops. The coolant of the second loop is sodium. The third loop is a steam turbine cycle. The key parameter of the system is the maximum temperature of $Li_{17}Pb_{83}$ at the outlet of the reactor chamber. It is taken to be 823 K. The inlet temperature of the eutectic is equal to 623 K. The inlet and outlet temperatures of sodium in the intermediate heat exchanger are 573 K and 773 K, respectively. In table 3, the mass flow rate and the pump power for liquid metal coolants are given.

The thermal scheme of the FIHIF power plant is presented in figure 10.

The steam cycle is configured with a reheat. The initial steam temperature and the reheat temperature are equal

to 743 K. The temperature of the feeding water is calculated to be 450 K. The efficiency of the steam cycle is equal to 0.407. Taking into account the driver efficiency, the target gain and the blanket multiplication for a fusion power of 1500 MW, we obtain a net efficiency of the plant of 0.373 and a net power per reactor of 626 MW.

8. Accelerator technology issues

The TeraWatt Accumulator project at ITEP, Moscow (ITEP-TWAC) takes advantage of an accelerator facility based on both synchrotron and storage rings (34 and 13 TM), with a non-Liouvillian stripping technique for stacking of the pulses accelerated in the UK booster synchrotron into the U10 storage ring [16]. Its aim is to produce a particle beam power of 1 TW with $\sim 10^{13}$ cobalt ions in bursts of 100 ns, accelerated to nearly 0.7 GeV u^{-1}.

Due to a very high aimed particle density in the phase space, many challenges in the accelerator physics and technology related to IFE should be addressed in this project:

(i) Efficient beam injection into the accelerator chain from an intense ion source capable of producing 10^{10}–10^{11} heavy ions in pulses of several microseconds at repetition rates of about 1 Hz.
(ii) A non-Liouvillian stacking technique is needed to accumulate a sufficient number of ions before extraction and irradiation of any experimental target.
(iii) A pulse compression of almost a factor of 10 in time has to be mastered just before the extraction.
(iv) Fast extraction, low-loss beam transport and focusing.
(v) Lifetime tests since an ultra-high vacuum must reduce the recombination of the ions circulating in the accumulator ring.

The ion accumulation procedure is based on charge-exchange injection using a fast bump system for minimizing the stacked beam perturbation by crossing the stripping foil material. A stripping target (5 mg cm^{-2} of Mylar) providing non-Liouvillian operation has been designed and installed. The whole acceleration/accumulation scheme has been tested by repetition of hundreds of pulse sequences for C^{6+} ions.

The beam accumulation test was carried out in the U10 ring with the RF on with a voltage of 1 kV and harmonic number 2 providing recapture of the injected beam, which had been bunched before in the booster synchrotron UK with harmonic number 10. The periodicity of the accelerating cycles was set to 3.5 s. Matching of the injected and stacked beams was reached by careful steering of the fast bump system, of the injected beam trajectory and of the orbit position to the stripping foil. As a result of the adjusting accumulator, the stacking process has been launched and the beam current in the U10 ring started to increase from cycle to cycle up to a level of 1.4×10^{10} (figure 11).

The accumulated bunch is compressed from 1 μs to $\sim$170 ns (FWHA) by the 10 kV/695 kHz RF bunch rotation technique.

As the repetition rate for the U10 multiple injection is less than 1 Hz, the required lifetime for the circulating beam has to be at least hundreds of seconds. As soon as the structure of the shielding chamber had been changed and the perturbing

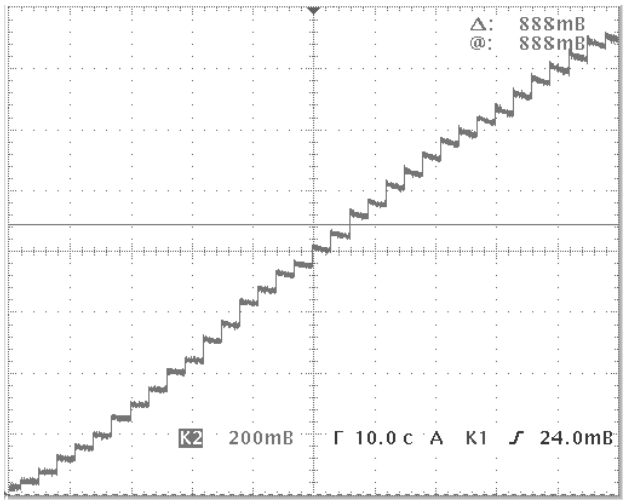

Figure 11. Linear growth of the C^{6+} beam intensity as a result of stacking in the accumulator ring.

field was eliminated, the beam circulation time increased to hundreds of seconds according to the vacuum conditions in the U10 ring.

An 86 m long new beamline for fast extraction to the beam–target interaction area has been constructed. The focusing elements and the interaction vacuum chamber are being fabricated and installed in the experimental area. The first beam–target interaction experiments using the γ-diagnostic with a beam focused onto a $\sim$1.5 mm spot have been performed.

By developing the stacking process in the accumulator ring U10, the basic non-Liouvillian stacking technique of the TWAC project can be successfully used for ion beam accumulation with increasing phase space density.

9. Conclusions

The FIHIF physical scenario based on the high-energy ion beam drive of a cylindrical target involves a realistic acceleration technology and a simple target design. The configuring of the reactor in two sections gives a possibility of increasing the rate of vapour condensation and reducing the vapour pressure loading. The problems of vapour fog in the chamber and pressure-stress pulsations in the blanket are a major concern for the reactor. The material limitations and tritium contamination of the coolant determine the thermodynamics of the thermal scheme. The balance of the plant is highly influenced by the driver energy consumption. Improvements in material characteristics and driver–target performance are needed to increase the efficiency of the power plant. The commissioning of the ITEP-TWAC facility opens a possibility of exploring critical accelerator technology issues relevant to IFE.

Acknowledgments

This work is sponsored in part by the Human Capital Foundation under contract N32. It is supported in part by the Program of Mathematical Department of the Russian Academy of Sciences N3 and by Minatom RF contract 2004/996.

References

[1] Lindl J.D. *et al* 2003 *Plasma Phys. Control. Fusion* **45** A217
[2] Meier W.R. *et al* 2003 *Fusion Eng. Des.* **62–63** 577
[3] Medin S.A. *et al* 2002 *Laser Part. Beams* **20** 419
[4] Medin S.A. *et al* 2003 *Fusion Sci. Technol.* **43** 437
[5] Basko M.M. *et al* 2004 *Phys. Plasmas* **11** 1577
[6] Basko M.M. *et al* 2002 *Laser Part. Beams* **20** 411
[7] Basko M.M. *et al* 2002 *Phys. Plasmas* **9** 1348
[8] Moir R.W. 1996 *Fusion Eng. Des.* **32–33** 93
[9] Hubbell J.H. and Seltzer S.M. 1995 Tables of x-ray mass attenuation coefficients and mass energy-absorption coefficients *Ionizing Radiation Division Report* S632 Institute of Standards and Technology Gaithersburg, MD 20899
[10] Medvedev A.B. 2004 Modification of the van der Waals model for dense states of matter *High Pressure Shock Compression of Solids VII, Shock Waves and Extreme States of Matter* ed V.E. Fortov *et al* (New York: Springer) chapter 13, p 531
[11] Rossi B. 1952 *High Energy Particles* (Englewood Cliffs, NJ: Prentice-Hall)
[12] Isachenko V.P. 1977 *Heat Transfer in Condensation Processes* (Moscow: Energia) (in Russian)
[13] GROUP-6 1981 MCNP—A General Monte Carlo Code for Neutron and Photon Transport, LA-7396-m Revised, Los Alamos National Laboratory (April 1981)
[14] Zinkle S.J. 1998 Status of recent activities by the APEX Material Group *APEX Study Meeting* Sundia National Laboratories, p 18
[15] Mikhailov V.N. *et al* 1999 *Lithium in Fusion and Space Power in 21st Century* (Moscow: Nauka) (in Russian)
[16] Alexeev N.N. *et al* 2002 *Laser Part. Beams* **20** 385
[17] Koshkarev D.G. 2002 Heavy ion driver for fast ignition *Laser Part. Beams* **20** 595